Generalized Scaling Laws of the Formation and Effects of Plasma-Confining Potentials for Tandem-Mirror Operations in GAMMA 10

T. Cho, J. Kohagura, T. Numakura, M. Hirata, H. Hojo, M. Ichimura, K. Ishii, A. Itakura, I. Katanuma, Y. Nakashima, T. Saito, Y. Tatematsu, M. Yoshikawa, R. Minami, S. Nagashima, M. Yoshida, T. Tamano, K. Yatsu, and S. Miyoshi
Plasma Research Centre, University of Tsukuba, Tsukuba, Ibaraki 305-8577, Japan
(Received 25 August 2000)

The main operations from 1979 to 2000 in the GAMMA 10 tandem-mirror, characterized in terms of the high-potential mode having kV-order plasma-confining potentials and the hot-ion mode yielding fusion neutrons with 10–20 keV bulk-ion temperatures, are summarized and generalized as a result of scalings of the formation and the effects of the potentials. The wide validity of potential-formation physics from Cohen's theory and the validity of the generalized Pastukhov's theory for the effects of thermal-barrier potentials on electron confinement are verified and consolidated through electron-energy balance.

DOI: 10.1103/PhysRevLett.86.4310 PACS numbers: 52.55.Jd, 52.50.Gj, 52.70.La

Extended investigations of the original scenario of potential-confined tandem-mirror plasmas with thermal barriers [1,2] require experimental verification of the potential-formation physics and the associated physical effects of the produced potentials on plasma-parameter improvement, so as to provide the essential physics bases for scaling construction and extension [1–5] (e.g., efficiency or various dependence studies of plasma parameters along these experimentally verified theoretical scaling bases, because of the inevitable necessity of potential confinement for mirror-fusion achievement [1,2]).

Even at this time, however, the physics-mechanism and scaling studies on the basis of the comparison between experimental data and potential theories [6–9] are reported in a limited number of publications for specific plasma operations alone [10–12].

In this Letter, from a large number of databases obtained from 1979 to 2000 in GAMMA 10, two representative operations characterized in terms of (i) a high-potential mode having kV-order plasma-confining potentials [10–12], and (ii) a hot-ion mode yielding fusion neutrons with 10–20 keV bulk-ion temperatures [13], are investigated. These data summaries are physically interpreted, combined, and then generalized under the proposed consolidation and combination of the two major theories of Cohen's strong electron-cyclotron heating (ECH) theory [6] and generalized Pastukhov's potential confinement theory [8,9] by the use of electron-energy and particle balance equations.

GAMMA 10 is a minimum-B anchored tandem mirror with outboard axisymmetric plug and barrier cells [5,10–14]. It has an axial length of 27 m, and the total volume of the vacuum vessel is 150 m^3. The central cell has a length of 6 m and a fixed limiter with a diameter of 36 cm, and the magnetic-field intensity at the midplane B_m is 0.405 T with a mirror ratio R_m of 5.2. Ion-cyclotron heatings (200 kW at 4.47 or 6.36 MHz, as well as 100 kW at 9.9 or 10.3 MHz) are employed for the central-cell hot-ion production and the anchor stabilization, respectively [13,14]. The plug and the barrier cells are axisymmetric mirrors; they have an axial length of 2.5 m ($B_m = 0.497$ T, and $R_m = 6.2$). Microwaves (150 kW at 28 GHz) are injected in the extraordinary mode into the plug and the barrier regions to produce an ion-confining potential ϕ_c, and a thermal-barrier potential ϕ_b, respectively.

Plug potentials Φ_P are measured with originally developed electrostatic spectrometer arrays for end-loss-ion analyses (ELA) [15]. Central-cell potentials Φ_C and barrier potentials Φ_B are directly measured with heavy-ion (Au^0) beam probes (HIBP) [16]. Thereby, we obtain ϕ_c and ϕ_b, as Φ_P-Φ_C and Φ_C-Φ_B, respectively. X-ray diagnostics give profiles of electron temperatures T_e along with detailed electron-energy spectra in each region [10–12,17].

In Figs. 1(a) and 1(b), scaling relations between ϕ_c and ϕ_b are summarized in the high-potential [10–12] and hot-ion modes [13], respectively. Both figures show a similarly behaved favorable increase in ϕ_c with increasing ϕ_b. Careful notices of the data in Figs. 1(a) and 1(b), however, find out a differently labeled ratio of the plug to central-cell densities, n_p/n_c, in each figure despite such similar behavior of ϕ_c with ϕ_b. In Fig. 1(a), plotted data have the values of n_p/n_c from 0.4 to 0.5, while in Fig. 1(b) data plotted with filled and open circles range in 0.07–0.10 and 0.10–0.13, respectively. This evidence seems to be contrary to the following predicted dependence of ϕ_c and ϕ_b on n_p/n_c from the strong ECH theory for the potential-formation mechanism [6]; that is,

$$\phi_c = T_e\left[0.665\left(\frac{n_p}{n_c}\right)\exp\left(\frac{1.19\phi_b}{T_e}\right)\right]^{2/3} - \phi_b\,, \quad (1)$$

where the units for the central-cell electron temperatures T_e and the potentials are in keV and kV, respectively.

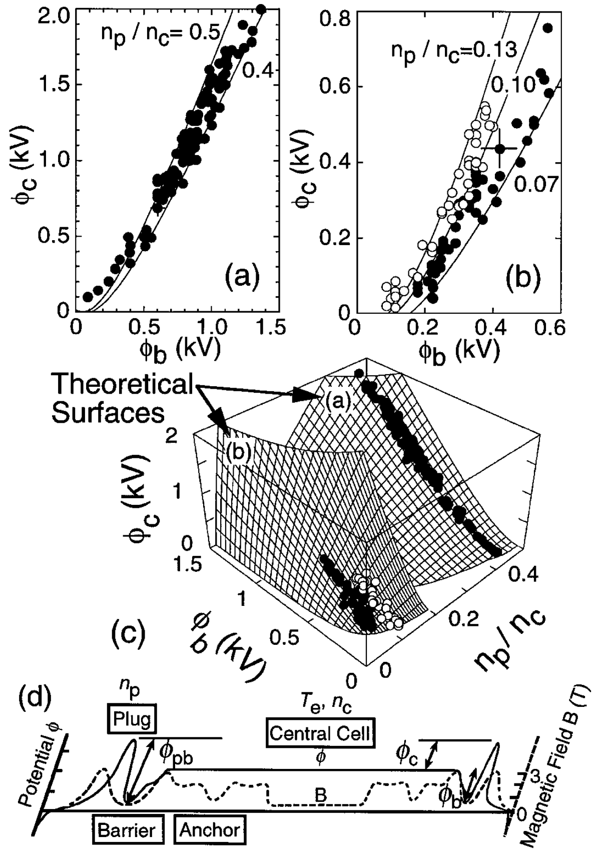

FIG. 1. The scaling laws of ϕ_c with ϕ_b in (a) the high-potential and (b) the hot-ion modes. The data having n_p/n_c in 0.4–0.5 for (a), as well as in 0.07–0.10 (filled circles) and 0.10–0.13 (open circles) for (b) are plotted. In (c), the generalized scaling surfaces (a) and (b) in the proposed three-dimensional space of ϕ_c, ϕ_b, and n_p/n_c are calculated from Cohen's strong ECH theory in combination with the scaling of T_c with ϕ_b [see Fig. 3 (below)]. The data in (a) and (b) are well replotted using the same symbols on the theoretical surfaces of (a) and (b) in (c), respectively. (d) Schematic view of axial magnetic-field and potential profiles in GAMMA 10 is depicted with notations of plasma parameters.

At this time, the strong ECH theory is believed to be the standard theory having the consistency with experimental data on tandem-mirror potentials [10,11]. Thus, the following systematic studies are carried out to address this serious problem. For plotting the solid curves labeled n_p/n_c in Fig. 1(a), an empirical relation of $T_e = 0.23\phi_b + 0.03$, obtained and approximated from the central-cell x-ray and HIBP data (for more detail, see below), is introduced to reduce T_e in Eq. (1). The curves consistently trace the data extended over $\phi_c = 2$ kV. The same method for interpreting the data in Fig. 1(b) is also applied because of no reports except for the high-potential mode. The substitution of the empirical scaling of $T_e = 0.16\phi_b + 0.01$ for the hot-ion mode similarly plots three curves labeled 0.07, 0.10, and 0.13, providing a finding of the recovery of good agreement between the experimental data and the strong ECH theory. In Fig. 1(c), the data sets of ϕ_c, ϕ_b, and n_p/n_c in Figs. 1(a) and 1(b) are replotted using the same symbols, lying well on each curved surface labeled (a) and (b), respectively. These methods and plots in the proposed three-dimensional space, thus, address the misunderstanding of no dependence of the relation between ϕ_c and ϕ_b on n_p/n_c. [For the notations of these parameters, see Fig. 1(d).]

For further investigations of the potential-formation mechanisms, an x-ray-energy spectrum in the plug region for the hot-ion mode is plotted in Fig. 2(a) using a specially developed semiconductor detector covering from a few hundred keV down to a few hundred eV [17]. Data in Fig. 2(a) are well traced by the calculated curve from the strong ECH theory. Here, the data of $2\phi_{pb} = 1.0$ kV measured with ELA and HIBP are employed for calculating the x-ray spectrum from the potential-trapped electrons [6,10,11], where ϕ_{pb} denotes the plug-electron confining potential of $\phi_c + \phi_b$. Also, the high-energy x-ray component is fitted using the mirror-trapped relativistic Maxwellian electrons (60 keV with a 35° loss cone, and 3.8% of the total plug density) [12] having the consistency with x-ray data in the barrier. In addition to the high-potential mode [10,11], a finding of good agreement between data and the strong ECH prediction even in the hot-ion model implies the existence of the common underlying physics in both representative modes in GAMMA 10.

In Fig. 2(b), the values of ϕ_{pb} deduced from the x-ray fittings, $\phi_{pb\text{-}x}$, viewing across the lines of magnetic force [0.94–1.1 T] are in good agreement with those from ELA and HIBP, $\phi_{pb\text{-EH}}$. The diagnostics characteristics of $\phi_{pb\text{-EH}}$ may leave room for argument on the location of Φ_p (e.g., at the mirror throat [18]) in the axial direction. In Fig. 2(b), however, good agreement of ϕ_{pb} measured from these two crossing directions confirms the location of Φ_p around 1 T, as predicted from the strong ECH theory. This evidence is also consistent with the decreasing axial potential profile from 1 T towards the mirror throat with electrostatic probe measurements.

Furthermore, the strong ECH theory predicts the relation between ϕ_{pb} (or ϕ_c) and ϕ_b as a function of n_p/n_c, without explicit dependence on n_c. In Fig. 2(c), data in the high-potential mode are distinguished by the triangles, squares, diamonds, and circles in n_c ranging (0.4–0.5), (0.5–0.6), (0.6–0.7), and $(1–2) \times 10^{18}$ m^{-3}, respectively. The data shown by the open symbols have $n_p/n_c = 0.4$. On the other hand, the strong ECH theoretical curves are represented by the dotted, solid, and dashed curves for n_p/n_c of 0.2, 0.4, and 0.6, respectively. It is found that the data having various values of n_c but the same value of n_p/n_c of 0.4 are well fitted by the theoretical curve with $n_p/n_c = 0.4$. This finding adds the evidence to verify the validity of the strong ECH theoretical bases. In Fig. 2(c), seven data shown by the filled symbols with the labeled values of n_p/n_c are plotted, where the shapes of the symbols are similary employed for distinguishing n_c. Wider validity of the theoretical dependence on n_p/n_c ranging in

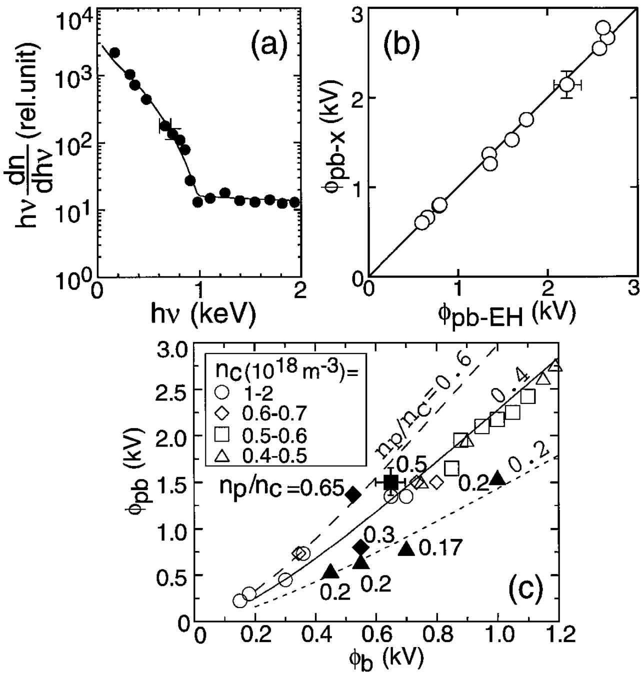

FIG. 2. (a) The plug x-ray spectrum in the hot-ion mode for $2\phi_{pb} = 1.0$ kV is fitted by the curve from the Cohen theory. (b) The data on ϕ_{pb} from the x-ray diagnostics, $\phi_{pb\text{-}x}$, viewing over the 0.94–1.1 T region are compared to those from ELA and HIBP, $\phi_{pb\text{-EH}}$. (c) In the high-potential mode, data on the relation between ϕ_{pb} and ϕ_b are distinguished by various symbols for n_c as labeled in the figure. Cohen's curves are represented by the dotted, solid, and dashed curves for $n_p/n_c =$ 0.2, 0.4, and 0.6, respectively. Open symbols having $n_p/n_c =$ 0.4 with various n_c, and seven filled symbols having the labeled n_p/n_c, are plotted and well fitted by the theory.

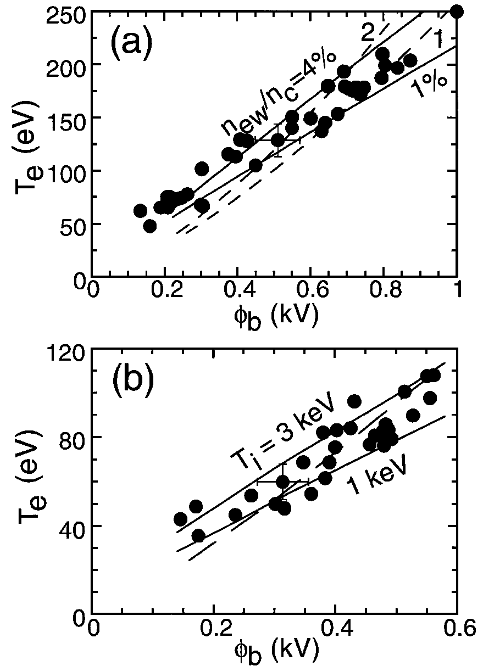

FIG. 3. The scalings of T_e with ϕ_b in (a) the high-potential and (b) the hot-ion modes are traced by the solid and dashed curves from Eqs. (2) and (3), respectively, using Pastukhov's energy- and particle-confinement times along with the labeled values of n_{ew}/n_c, T_i, or n_0 [1 and 2 in (a) corresponding to 1 and 2 × 10^{15} m^{-3}, respectively, and in (b) being 2 × 10^{15} m^{-3}] (see text). In (a), data with $T_{ew} = 1$–2 keV, $n_{ew}/n_c = 1\%$–5% [$n_c = (4$–$6) \times 10^{17}$ m^{-3}], $T_i = 2$ keV, and $n_0 = (1$–$4) \times 10^{15}$ m^{-3}; and in (b), data with $T = 1$–5 keV, $n_c = (1$–$2) \times 10^{18}$ m^{-3}, and $n_0 = (1$–$4) \times 10^{15}$ m^{-3} are plotted.

0.17–0.65 beyond the typical operational regime of n_p/n_c of 0.4–0.5 in the high-potential mode is also found.

The next issue is to clarify the predominant factor in determining T_e. This has been one of the unresolved problems in tandem mirrors. Moreover, the above-described two empirical relations between T_e and ϕ_b obtained from the data fitting have to be physically interpreted for generalizing the proposed three-dimensional plots in Fig. 1(c) for exploring the future alternative operational regime.

In Figs. 3(a) and 3(b), the scaling of T_e with ϕ_b on the magnetic axis are plotted in the high-potential and hot-ion modes, respectively. In Fig. 3(a), data with the warm-electron temperatures $T_{ew} = 1$–2 keV and the density ratio $n_{ew}/n_c = 0.01$–0.05 to $n_c = (4$–$6) \times 10^{17}$ m^{-3} are plotted. (For the T_e analyses and distribution functions, see Refs. [8], [10], and [11].) Ion temperatures $T_i =$ 2 keV, and the neutral-particle populations $n_0 = (1$–$4) \times$ 10^{15} m^{-3} are observed. Here, n_0 decreases with increasing T_e. In Fig. 3(b), data having $T_i = 1$–5 keV, $n_c =$ $(1$–$2) \times 10^{18}$ m^{-3}, $n_0 = (1$–$4) \times 10^{15}$ m^{-3}, and $T_{ew} =$ 1 keV with $n_{ew}/n_c = 0.005$–0.01 are plotted.

The theoretical analyses from the above viewpoints are carried out by the use of the energy- and particle-balance Eqs. (2) and (3), respectively:

$$\frac{dWV_{BB}}{dt} = P_{wb}V_{BB} + P_{hb}V_h - \frac{WV_{BB}}{\tau_E}, \qquad (2)$$

and

$$\frac{dn_c}{dt} = n_0 n_c \langle \sigma \nu \rangle - \frac{n_c}{\tau_p}, \qquad (3)$$

where W and $\langle \sigma \nu \rangle$ denote the bulk-electron energy density of $\frac{3}{2}n_c T_e$, and the ionization cross section, respectively. Slowing-down power densities to the bulk electrons from the warm electrons, and the hot ions are defined as P_{wb} and P_{hb}, respectively. The volume of the warm electrons, flowing from the plug region and thus existing between both barrier regions, is represented by V_{BB} [10]. Diamagnetic-loop-array signals for hot-ion profile measurements are analyzed to identify the axial profile [19] and the volume of hot ions V_h.

In Fig. 3(a), the solid curves labeled $n_{ew}/n_c = 1$ and 4% having T_{ew} of 1 keV are calculated from Eq. (2) with the substitution of generalized Pastukhov's energy-confinement time modified by Cohen *et al.* [8] into τ_E. Here, the second term of the right-hand side of Eq. (2) is 1 order of magnitude smaller than the first term (2 keV ions with V_h/V_{BB} of 0.39). The dashed curves are simulated from Eq. (3) with Pastukhov's particle-confinement time [8,9] into τ_p. The tendency of an increasing neutral-shielding effect with increasing T_e or ϕ_b is seen by the data from $\phi_b \approx 0.8$, through 0.5, and then to 0.2 kV, since these data are traced by the dashed curves labeled 1 and 2 (corresponding to $n_0 = 1$, and 2×10^{15} m^{-3}, respectively), and then the calculations with poorer shielding with $n_0 \approx 5 \times 10^{15}$ m^{-3}, respectively. This behavior is consistently understood by the dependence of $\langle \sigma v \rangle$ on T_e.

Similarly, data in Fig. 3(b) are also fitted by the calculated solid curves from Eq. (2) with $T_i = 1$ and 3 keV along with $n_c = 1.5 \times 10^{18}$ m^{-3}. In contrast to the parameter regime in Fig. 3(a), $P_{hb} V_h$ dominates over $P_{wb} V_{BB}$. In Fig. 3(b), the dashed curve is similarly estimated from Eq. (3) by the use of the averaged data of $n_0 = 2 \times 10^{15}$ m^{-3} and the above-described parameters.

Good agreement between the data and the calculated results in each different parameter regime with the different dominant-heating source in Figs. 3(a) and 3(b) confirms the simultaneous validity of Eqs. (2) and (3) along with the generalized Pastukhov theory for the confinement of the central-cell bulk electrons. (The results from various modifications of Pastukhov's theory [9,20,21] range in the present data plots within the error bar.)

In this context, we investigate to find the general formula for the relation between T_e and ϕ_b on the basis of the combination of the energy-balance equation with the Pastukhov energy confinement time in place of the two experimentally obtained empirical scalings of T_e with ϕ_b employed in Fig. 1.

In a quasisteady state, one can obtain the following equation when equalizing τ_E from the generalized Pastukhov theory with τ_E in the energy-balance equation:

$$\frac{7.48 \times 10^{-5} \frac{T_e^{3/2}}{n_c \ln\Lambda} x \exp(x) \frac{1}{I(x^{-1})}}{\frac{2}{3} x \frac{1}{I(x^{-1})} + 1} = \frac{\frac{3}{2} n_c T_e}{\frac{V_h}{V_{BB}} P_{hb} + P_{wb}}, \tag{4}$$

where $I(x)$ is well approximated by $(1 + x/2)/(1 + x^2/4)$ with $x = \phi_b/T_e$ [8,9]. By the use of $f(x) = [x \exp(x)]/[\frac{2}{3}x + I(x^{-1})]$, Eq. (4) is written as

$$f(x) = \frac{2.01 \times 10^4 n_c^2 \ln\Lambda}{T_e^{1/2}[\frac{V_h}{V_{BB}} P_{hb} + P_{wb}]}, \qquad \text{or}$$

$$x = \frac{\phi_b}{T_e} = f^{-1}\left[\frac{2.01 \times 10^4 n_c^2 \ln\Lambda}{T_e^{1/2}[\frac{V_h}{V_{BB}} P_{hb} + P_{wb}]}\right], \tag{5}$$

where the units of T_e, ϕ_b, n_c, P_{hb}, and P_{wb} are in keV, kV, 10^{18} m^{-3}, W $\times$ m^{-3}, and W $\times$ m^{-3}, respectively.

From the generalized Eq. (5), one can reproduce the above-mentioned two empirical scalings of T_e with ϕ_b. A finding of a good approximation of $f^{-1}(x) \approx 0.04 + 0.97 \ln[f(x)]$, along with the substitution of standard formula for P_{hb} and P_{wb}, allows us to derive the above-employed empirical formula of $\phi_b \approx 1.33 + 4.39(T_e - 0.33)$ with the Taylor expansion in the above-described parameter regime of the high-potential mode [Fig. 1(a)], for instance.

In summary, in combination with the theoretical generalization and interpretations of the empirical scaling relations between T_e and ϕ_b through the electron energy-balance treatment due to the generalized Pastukhov potential-confinement mechanisms [Eq. (5) for the generalization of the above empirical scalings of T_e with ϕ_b], the potential-formation scalings in the representative tandem-mirror operational modes [Figs. 1(a) and 1(b)] are generalized and consolidated [Fig. 1(c) with Fig. 3 or Eq. (5)] on the basis of the findings of wider validity of Cohen's strong ECH theory (Figs. 1 and 2). Accordingly, the present investigations, providing an opportunity to combine and consolidate these two major theories for the potential formation and the associated potential confinement of tandem-mirror plasmas, may give the bases for exploring the future developing operations extended from the present database [22].

[1] R. F. Post, Nucl. Fusion **27**, 1579 (1987), a review paper of tandem mirrors.

[2] D. E. Baldwin and B. G. Logan, Phys. Rev. Lett. **43**, 1318 (1979); G. I. Dimov *et al.,* Sov. J. Plasma Phys. **2**, 326 (1976); T. K. Fowler and B. G. Logan, Comments Plasma Phys. Control. Fusion **2**, 167 (1977).

[3] D. D. Ryutov, in *Proceedings of the International Conference on Plasma Physics, New Delhi, 1989* (IAS, Bangalore, 1989).

[4] N. Hershkowitz, S. Miyoshi, and D. D. Ryutov, Nucl. Fusion **30**, 1761 (1990).

[5] S. Miyoshi *et al.,* Fiz. Plazmy **23**, 781 (1997) [Plasma Phys. Rep. **23**, 723 (1997)].

[6] R. H. Cohen, Phys. Fluids **26**, 2774 (1983).

[7] R. H. Cohen *et al.,* Nucl. Fusion **20**, 1421 (1980); **23**, 1301 (1983).

[8] V. P. Pastukhov, Nucl. Fusion **14**, 3 (1974).

[9] R. H. Cohen, M. E. Rensink, T. A. Cutler, and A. A. Milin, Nucl. Fusion **18**, 1229 (1978); R. H. Cohen, *ibid.* **19**, 1295 (1979); **19**, 1693 (1979).

[10] T. Cho *et al.,* Phys. Rev. Lett. **64**, 1373 (1990).

[11] T. Cho *et al.,* Phys. Rev. A **45**, 2532 (1992).

[12] T. Cho *et al.,* Nucl. Fusion **27**, 1421 (1987).

[13] Y. Kiwamoto *et al.,* Phys. Plasmas **3**, 578 (1996).

[14] M. Ichimura *et al.,* Nucl. Fusion **39**, 1995 (1999).

[15] Y. Sakamoto *et al.,* Rev. Sci. Instrum. **66**, 546 (1995).

[16] K. Ishii *et al.,* Rev. Sci. Instrum. **60**, 3270 (1989).

[17] J. Kohagura *et al.,* Rev. Sci. Instrum. **66**, 2317 (1995).

[18] M. R. Carter, TMX-U Final Report, UCID-20981 (1988), Vol. 1, p. 120.

[19] I. Katanuma *et al.,* Jpn. J. Appl. Phys. **27**, 159 (1988).

[20] F. Najmabadi, R. W. Conn, and R. H. Cohen, Nucl. Fusion **24**, 75 (1984).

[21] V. N. Khudik, Nucl. Fusion **37**, 189 (1997).

[22] T. Cho *et al.,* in *Proceedings of the 18th International Conference on Fusion Energy, Sorrento, 2000* (International Atomic Energy Agency, Vienna, 2001).